Optik - International Journal for Light and Electron Optics 184 (2019) 90–97

Contents lists available at ScienceDirect

Optik

journal homepage: www.elsevier.com/locate/ijleo

Original research article

Full-stainless steel mesh dye-sensitized solar cells based on core-shell ZnO/TiO_2 nanorods

Lei Sheng[a], Gang Li[a], Wendong Zhang[a], Kaiying Wang[a,b,*]

[a] MicroNano System Research Center, College of Information and Computer & Key Lab of Advanced Transducers and Intelligent Control System (Ministry of Education), Taiyuan University of Technology, Taiyuan, 030024, China
[b] Department of Microsystems-IMS, University of South-Eastern Norway, Horten, 3184, Norway

ARTICLE INFO

Keywords:
Flexible dye-sensitized solar cells
Core-shell
Full stainless steel mesh
Reflecting film

ABSTRACT

We report fabrication and photovoltaic properties of flexible dye-sensitized solar cells (FDSSCs) based on stainless steel mesh (SSM)-supported core-shell ZnO/TiO_2 nanorods photoanode and Pt nanoparticles- coated SSM counter electrode (Pt/SSM CE). The core-shell ZnO/TiO_2 structures were prepared via simple chemical bath deposition, and optimal conversion efficiency of 2.84% was achieved. When aluminum foil membrane was introduced on the back of the FDSSCs as reflecting film (Rf) for improving utilization of sunlight, the conversion efficiency of FDSSCs was increased from 2.84% to 3.12%. The relative improvement of 218% was achieved in conversion efficiency compared with similar device without TiO_2 buffer layer and reflecting film (0.98%). Meanwhile, the Pt CE based on SSM possessed of higher catalytic ability and longer stability compared with ITO/PET-based Pt CE.

1. Introduction

Flexible dye-sensitized solar cells (FDSSCs) have been considered as promising device in the field of portable power [1–6]. Nowadays, TiO_2 is the most effective material for photoanode due to its excellent electron mobility, good acid resistance and remarkable adsorption with dye molecules [7–12]. However, the application of TiO_2 in flexible DSSCs has been limited due to the extreme condition for growing TiO_2 nanostructures [13]. Moreover, low heat-proof temperature of plastic conductive substrates also constraints fabrication and post-treatment process of flexible photoanode [14–17]. Meanwhile, the Pt counter electrode based on plastic substrate often suffers from non-uniform distribution of Pt particles and poor mechanic stability [18–20]. These obstacles above result in high cost and complicated process, thus hindering FDSSCs' development.

Hence, the FDSSCs based on ZnO and flexible metal substrate has attracted wide attention due to their characteristics, such as ZnO's approximate band gap energy with TiO_2, high electron mobility (115–155 $cm^2.V^{-1}.s^{-1}$), large excitation binding energy (60 eV), high availability at low-cost and richer morphologies [21]. In particular, the ZnO FDSSCs based on SSM has been a research hotspot for economic and easy-manufacture FDSSCs because of its low cost, excellent flexibility, less technical requirement and stable interconnection between ZnO NRs and SSM [22,23]. For instance, Lu et al. prepared the FDSSCs consisting of a SSM-supported ZnO NRs photoanode and yielded a conversion efficiency of 1.11% [24], Dai et al. fabricated the FDSSCs based on SSM-supported ZnO nanowire array and attained a conversion efficiency of 1.87% [25]. Unfortunately, the FDSSCs with ZnO/SSM photoanode always achieve low conversion efficiency, which results from the dissolution of ZnO to Zn^{2+} by the acidic dye (such as N3, N719, and black

* Corresponding author at: MicroNano System Research Center, College of Information and Computer & Key Lab of Advanced Transducers and Intelligent Control System (Ministry of Education), Taiyuan University of Technology, Taiyuan, 030024, China.
E-mail address: Kaiying.Wang@usn.no (K. Wang).

https://doi.org/10.1016/j.ijleo.2019.03.025
Received 4 December 2018; Received in revised form 24 February 2019; Accepted 9 March 2019

dye), the formation of insulating layer consisting of agglomerates of Zn^{2+} and dye molecules (blocking the electrons injection to the semiconductor) and high light loss from mesh pore [26,27].

It is worth mentioning, Dai et al. confirmed that TiO_2 buffer layer prepared via atomic layer deposition (ALD) is an effective strategy for improving performance and weakening acidic corrosion [28]. To increase cost-efficiency of FDSSCs based on ZnO/SSM, a simplified method ($(NH_4)_2TiF_6$ treatment) was introduced to prepare TiO_2 buffer layer on ZnO NRs for improving conversion efficiency. Meanwhile, the Pt CE with uniform distribution is prepared on SSM for high performance. In order to an improvement further, aluminum foil also was employed to decrease the loss of sunlight from mesh pores. Thus, the performance of ZnO-based FDSSCs is improved significantly under low cost and easy process, which will promote its development.

2. Experiment

2.1. Materials and reagents

All chemical reagents were of analytical grade, including sodium hydroxide (NaOH), zinc acetate dehydrate ($Zn(CH_3COO)_2$. $2H_2O$), boric acid (H_3BO_3), lithium iodide (LiI) ammonium hexafluorotitanate ($(NH_4)_2TiF_6$), hydrochloric acid (HCl), iodide (I_2), chloroplatinic acid (H_2PtCl_6), 4-tert-butylpyridine (TBP), 1-Methyl-3-propylimidazolium Iodide (MPII), absolute ethyl alcohol and acetonitrile, purchased from Sinopharm Chemical Reagent Co., Ltd. The sensitizer (N719) had bought from Chinese YingKou OPV Tech New Energy Co., Ltd. And other materials which will be employed contain SSM (model of 304, 25 μm wire diameter and 20 μm screen opening), ITO/PET (6 Ω/cm^2) and PET film.

2.2. Preparation of ZnO nanorod and TiO_2 coated ZnO nanorod on SSM

At first, SSM is tailored to 2 × 2cm^2 size, submerged in HNO_3 (4 M) at 70℃ for 4 h to remove surficial impurity and then cleaned through ultrasonic bath in ethyl alcohol, deionized water for 10 min respectively. The ZnO seed layer is vital to grow ordered ZnO nanorods on SSM. Therefore, ZnO seed layer was prepared on SSM via submerging SSM in ethyl alcohol solution of zinc acetate (0.01 M) for 30 s and annealing at 300℃ for 10 min, repeated 3 times.

Then SSM supported ZnO NRs (ZnO NRs/SSM) was prepared by hydrothermal method. Namely, SSM with seed layer were putted in autoclave with 60 ml solution included 0.05 M zinc acetate and 1 M NaOH, kept at 95℃ for 18 h. Next, samples were washed in deionized water and dried at 60℃ for 30 min. Subsequently, the ZnO NRs/SSM was placed in closed flask contained $(NH_4)_2TiF_6$ (0.75 M) and H_3BO_3 (0.2 M) mixed solution of 50 ml, subjected for different duration of time (0, 3, 6, 9, 12 min) to prepare TiO_2 buffer layer-coated ZnO/SSM (TiO_2/ZnO NRs/SSM) [29]. Finally, these samples were washed in deionized water and then sintered at 450℃for 2 h.

2.3. Assembly of FDSSCs

TiO_2/ZnO NRs/SSMs were placed in dye solution, which attained by dissolving 18 mg N719 in 50 ml ethyl alcohol, and then kept in dark at 40℃ for 24 h. The sensitized samples were rinsed with deionized water and dried at 60℃ for 30 min.

The Pt/SSM and Pt/ITO/PET CE were fabricated via cyclic voltammetry which is implemented in the aqueous electrolyte consisted of H_2PtCl_6 (0.75 wt%) and HCl (1.43 vol%). In this process, the applied potential, scan rate and cycles were set as between −0.4 V and 0.5 V, 10 mV/s and 5 cycles, respectively. Moreover, clean substrates (SSM and ITO/PET), platinum mesh and saturated calomel electrode (SCE) were used as working, counter and reference electrode separately. After that, the samples were rinsing with deionized water, dried at 80℃ for 30 min, and then tailored to suitable size. Finally, as-prepared photoanode was assembled with CE in a sandwich structure, and then the electrolyte (LiI of 0.1 M, I_2 of 0.05 M, TBP of 0.5 M and MPII of 0.6 M in acetonitrile.) was injected in these devices.

2.4. Characterization and measurement

The morphology and structure of the ZnO NRs/SSM and TiO_2/ZnO NRs/SSM were studied by field-emission scanning electron microscopy (FE-SEM, SU-3500) and transmission electron microscope (TEM, Tecnai G2-F20). The crystalline phase of the samples was examined through X-ray diffraction (XRD, Bruker-D8 ADVANCE) with a monochromatic Cu Ka irradiation (λ = 0.154145 nm). The photocurrent-voltage (J–V) curve of the SSM-based FDSSCs were measured by a source meter (Keithley 2400) under AM 1.5 G illumination (100 mW/cm^2) from a Newport Oriel solar simulator in ambient atmosphere. In terms of FDSSCs' active area of 1.46 cm^2, four major indexes of the FDSSCs, such as photocurrent density of short circuit (J_{sc}), voltage of open circuit (V_{oc}), fill factor (FF) and conversion efficiency (η), were obtained.

3. Result and discussion

3.1. TiO_2 buffer layer

ZnO NRs were synthesized on ZnO seed layer-coated SSM by a simple hydrothermal method. Fig. 1(a) shows morphology of pure ZnO NRs at different magnification. Fig. 1(b–d) present the cross section of pure ZnO NRs/SSM. From Fig. 1(b), it can be observed

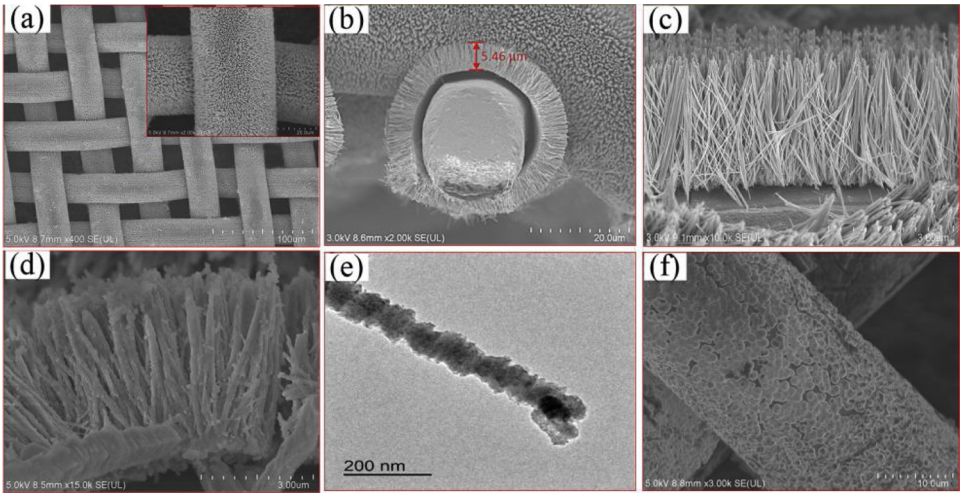

Fig. 1. (a) SEM images of SSM-supported pure ZnO NRs, (b–c) cross section of SSM supported pure ZnO NRs at different magnification, (d) cross section of SSM-supported ZnO NRs with $(NH_4)_2TiF_6$ treatment of 12 min, (e) TEM image of the ZnO NR with $(NH_4)_2TiF_6$ treatment for 12 min,(f)SEM image of Pt/SSM CE.

that the length of ZnO NRs is about 5.46 μm, and vertically grow on SSM. The morphology of ZnO NRs/SSM after $(NH_4)_2TiF_6$ treatment of 12 min is exhibited in Fig. 1(d). The chemical reactions occurring in treatment process might follow next three EQs [30]:

$$TiF_6^{2-} + 2H_2O \rightarrow TiO_2 + 4H^+ + 6F^- \quad (1)$$

$$BO_3^{3-} + 4F^- + 6H^+ \rightarrow BF_4^- + 3H_2O \quad (2)$$

$$ZnO + 2H^+ \rightarrow Zn^{2+} + H_2O \quad (3)$$

In this treatment, the surface of ZnO NSs was dissolved into the solution. Meanwhile, the TiO_2 was grown in situ on the ZnO NRs surfaces. As a result, a thin TiO_2 layer was coated on the ZnO NRs, and the surface of TiO_2/ZnONRs gets rough (Fig. 1(e)). And Fig. 1(f) exhibited the uniform distribution of Pt nanoparticles on the SSM surface. Fig. 2(a) shows EDS spectrums of the $(NH_4)_2TiF_6$-treated ZnO NRs film. The peaks at 4.49 and 4.92 keV correspond to the Ti, which verifies the formation of TiO_2 on ZnO NRs surfaces. The peaks at Ca. 6.38 and 7.14 keV represent Fe, Ni, respectively. The Fe and Ni derive from SSM.

Fig. 2(b) shows the XRD pattern of the ZnO NRs before and after a $(NH_4)_2TiF_6$ treatment of 6 min. In the image, green and red line exhibits untreated ZnO NRs, $(NH_4)_2TiF_6$-treated ZnO NRs respectively. Compared with green diffraction peaks, red diffraction peaks appear in (101), (200) and (204) peak, which confirmed that ZnO NRs/SSM is coated with TiO_2 layer. There is no notable change among red and green (111), (200) and (220) peaks, which illustrates substrate has no obvious variation before and after $(NH_4)_2TiF_6$ treatment. However, obvious weakness can be observed in red (100), (101) and (110) peak compared with corresponding green peaks. This phenomenon also verifies that the growth of TiO_2 layer is based on the sacrifice of ZnO. Meanwhile, the slight decline of (002) peak and the disappearance of (103) peak indicates non-uniform growth of TiO_2.

Fig. 3(a) shows SEM image of $(NH_4)_2TiF_6$-treated ZnO NR. It can be observed that the $(NH_4)_2TiF_6$-treated ZnO NR exhibits unsmooth surface, which is possibly result from nonuniform growth of TiO_2. Fig. 3(b) presents element mapping of major elemants

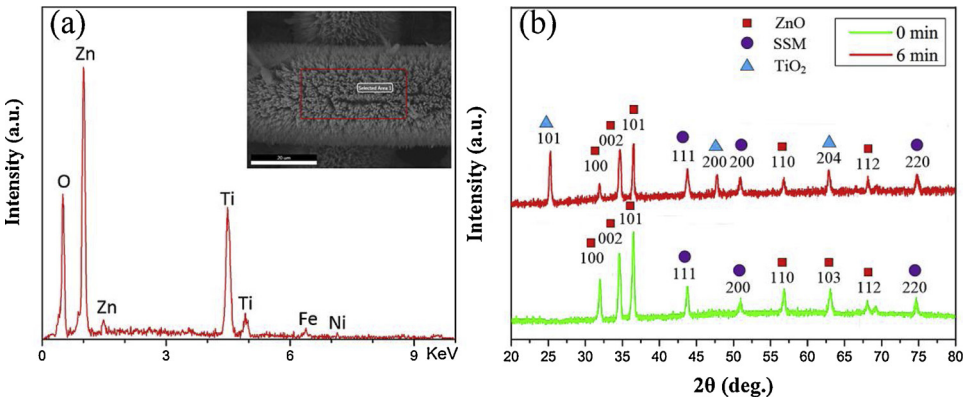

Fig. 2. (a) EDS of ZnO NRs/SSM with $(NH_4)_2TiF_6$ treatment and (b) XRD of ZnO NRs/SSM with $(NH_4)_2TiF_6$ treatment for different time.

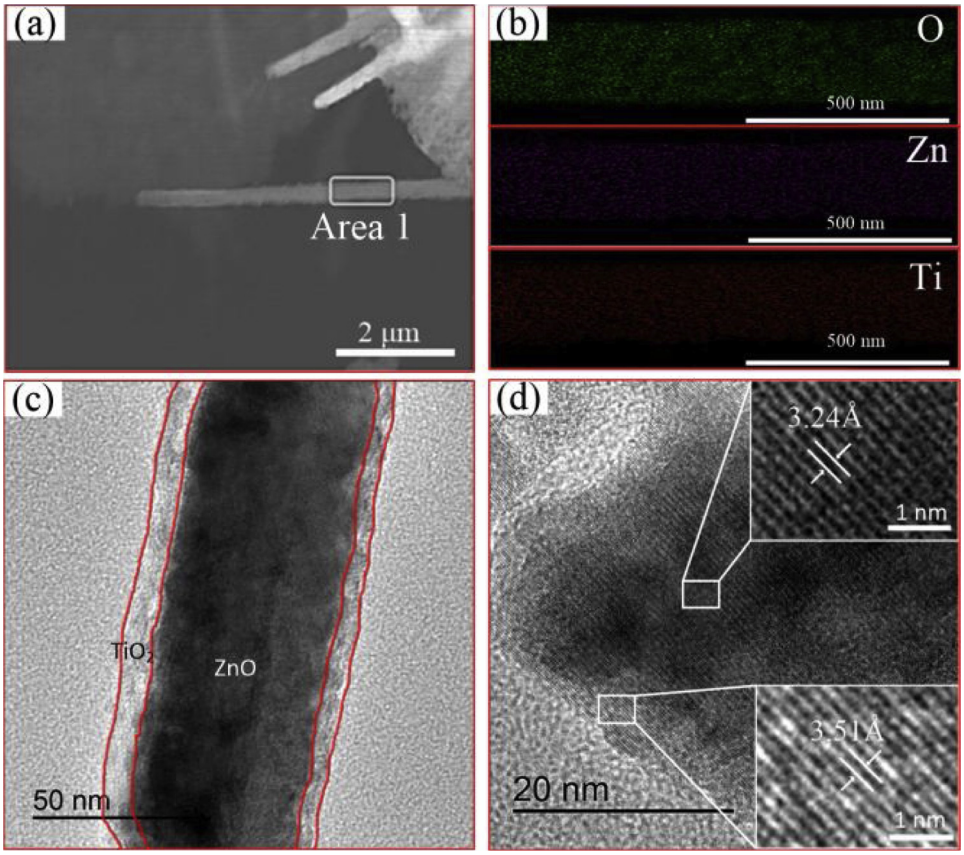

Fig. 3. (a) SEM of ZnO NRs/SSM treated with (NH4)2TiF6 solution for 6 min, (b) corresponding element mapping image of area 1, (c) TEM and (d) HRTEM of single ZnO NRs with $(NH_4)_2TiF_6$ treatment of 6 min.

(O, Zn, Ti) corresponding to arae 1, which TiO_2 is fully coated on the surfce of ZnO NRs. TEM (Fig. 3(c)) and HRTEM (Fig. 3(d)) also confirm that TiO_2 is coated on ZnO NRs completely, but coated layer isn't uniform (namely rough surface). In certain degree, this rough surface of TiO_2-coated ZnO NRs can increase surface area and dye-adsorbing capacitiy, thus improving photocurrent intensity [31,32].

Fig. 4(a) shows the photocurrent intensity-voltage curves of the FDSSCs consisted of Pt/SSM CE and TiO_2/ZnO NRs/SSM photoanode which was treated in $(NH_4)_2TiF_6$ solution for 0, 3, 6, 9, 12 min respectively. Those characteristic parameter (J_{sc}, V_{oc} and FF) corresponding to the performance curves of FDSSCs are listed in the Table 1. The FDSSCs based on pure ZnO NRs/SSM photoanode exhibited conversion efficiency of 0.98%, J_{sc} of 4.61 mA/cm^2, V_{oc} of 0.49 V and FF of 0.43. After $(NH_4)_2TiF_6$ treatment of 3 min, the V_{oc}, J_{sc} and FF of the FDSSCs were improved to 0.59, 6.32 mA/cm^2 and 0.52, respectively. The J_{sc} of device increased to the 7.22 mA/cm^2 after treatment of 6 min. And the V_{oc} and FF reached to 0.61 V, 0.64 respectively. Thus, the conversion efficiency also increased to 2.84% from 0.98%, which confirms that TiO_2 buffer layer is effective to enhance performance of ZnO FDSSCs. It is possible that this improvement results from the suppression of the photoexcited electron recombination and promotion of electron collection [33]. Fig. 4(b) shows the dark current curves of various FDSSCs. compared with the device without $(NH_4)_2TiF_6$ treatment, the devices with $(NH_4)_2TiF_6$ treatment exhibit smaller dark current, which suggests effectively that TiO_2 buffer layer can suppress the electron recombination at the interface between nanorod and electrolyte.

With treatment of 6 min, the V_{oc}, J_{sc} and FF of the FDSSCs reach to maximum. Subsequently, the J_{sc} shows slight reduction with the increase of treatment time. Fig. 4(c) exhibits IPCE curves of the devices with deferent treatment time, which also confirm this situation. The slight reduction of J_{sc} possibly results from the increase of TiO_2 thickness. Namely, TiO_2 thickness increased with increasing treatment time due to TiO_2 deposition effect, thus reduce and block the space which is likely to anchor dye molecules among nanorods. Moreover, thick TiO_2 layer hindered electron collection [34,35]. Therefore, the conversion efficiency shows slight decline.

The EIS of DSSC with different electrolytes (exhibited in Fig. 4(d)) are fitted with equivalent circuit (insert image of Fig. 4(d)), and charge transfer resistance of DSSCs are summarized in Table 2. In EIS spectra, R_s refers to the series resistance of the electrolytes and electric contacts in the DSSCs. R_1 and R_2 correspond to the charge transfer processes occurring at the counter electrode/electrolyte (first arc), photoanode/electrolyte interface (second arc), respectively. Therefore, the values of R_2 can evaluate the electron collection and recombination of photoanode [36].

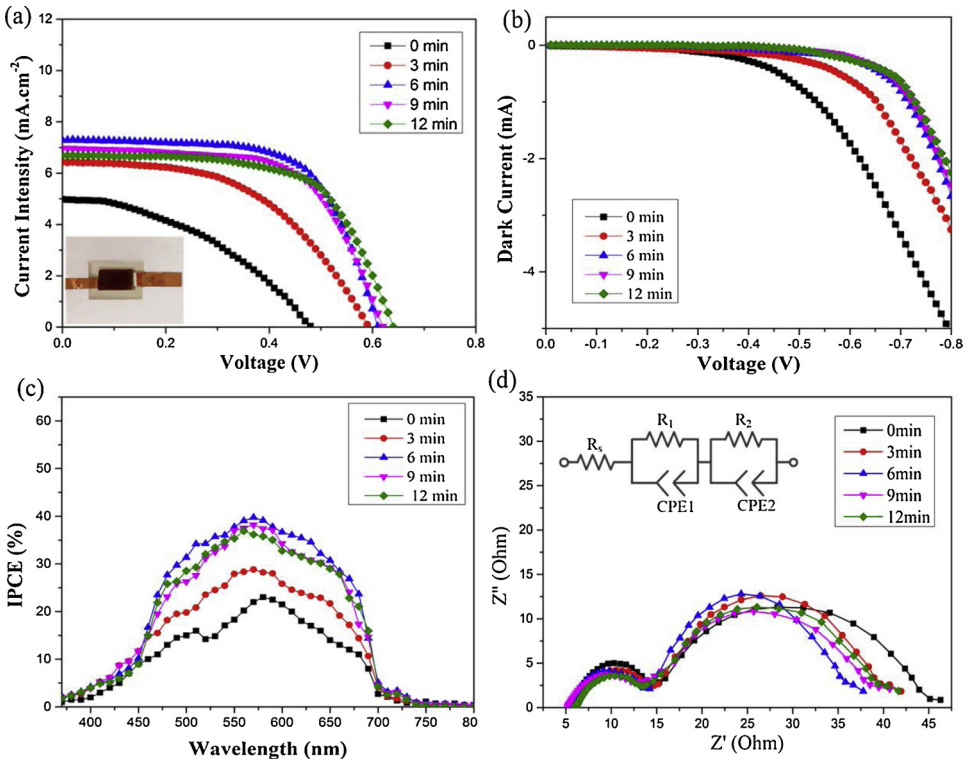

Fig. 4. (a) Photocurrent density-voltage, (b) dark current and (c) incident monochromatic photon conversion efficiency (IPCE) curves of the flexible DSSCs with the photoanodes based on ZnO NRs/SSM with different $(NH_4)_2TiF_6$ treatment time, (d) EIS of FDSSCs with deferent treatment time.

Table 1
Photovoltaic characteristics of the DSSCs using the photoanodes based on ZnO NRs/SSM with different $(NH_4)_2TiF_6$ treatment time.

Treatment time	V_{oc} (V)	J_{sc} (mA. cm^{-2})	FF	Efficiency (%)
0 min	0.491	4.61	0.43	0.98
3 min	0.592	6.32	0.52	1.93
6 min	0.611	7.22	0.64	2.84
9 min	0.624	6.95	0.62	2.70
12 min	0.643	6.69	0.62	2.69

Table 2
Electrochemical parameters of FDSSCs with various treatment durations.

Treatment time	R_S/Ω	R_1/Ω	R_2/Ω
0min	5.91	8.55	29.85
3 min	6.15	8.61	26.21
6 min	5.39	8.91	22.52
9min	5.23	8.12	25.88
12 min	6.08	8.01	27.08

It is found from Table 2 that, the FDSSCs without treatment have the highest R_2 of 29.85Ω. The FDSSCs with treatment of 6 min show the lowest R_2 (22.52Ω). The FDSSCs treated for 3 min, 9 min and 12 min possess R_2 of 26.21Ω, 25.88Ω and 27.08Ω, respectively. The FDSSCs with TiO_2 buffer layer exhibit lower R_2 than that without buffer layer, which verified that the TiO_2 buffer layer can promote electron collection [37]. Meanwhile, the devices treated for 9 min and 12 min exhibit larger R_2 than the device treated for 6 min, which verifies thick TiO_2 layer hinders electron collection.

3.2. Reflecting film

Fig. 5(a) shows the photocurrent-voltage curves for the FDSSCs which employed TiO_2/ZnO NRs/SSM photoanodes ($(NH_4)_2TiF_6$ treatment of 6 min) and different CEs with as well as without reflecting film. Characteristic parameters corresponding to those curves

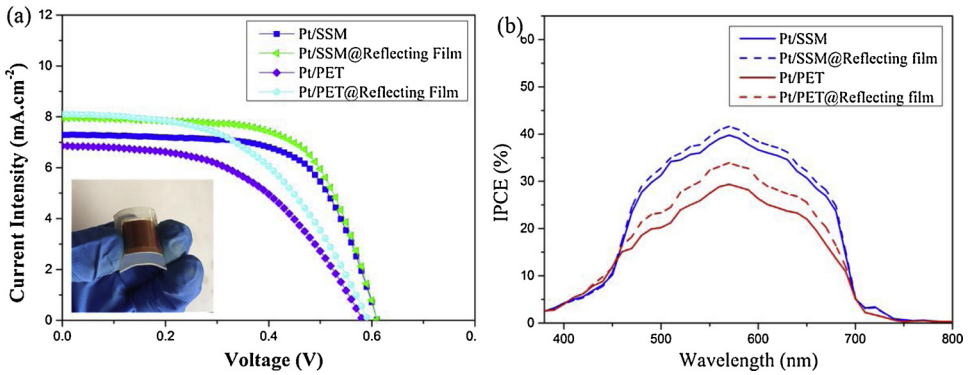

Fig. 5. (a) Photocurrent density-voltage curves and (b) IPCE of the flexible DSSCs employing different CEs with and without reflecting film (Al foil) on its back.

were summarized in Table 3. The FDSSCs with Pt/SSM CE, Pt/PET CE show conversion efficiency of 2.84%, 2.02%, respectively.

After utilization of Rf, the J_{sc} of FDSSCs employing different CE increased from 7.22 mA/cm^2, 6.43 mA/cm^2 to 7.94 mA/cm^2, 8.1 mA/cm^2, respectively. But corresponding V_{oc} and FF almost have no change, possibly resulting from the improvement of the light-absorbing and light-transferring capability under the utility of reflecting film. However, the improvement of FDSSCs with Pt/SSM CE (9%) was lower than that of FDSSCs employing Pt/PET CE (21%). The corresponding IPCE (shown in Fig. 5(b)) also confirmed same situation. The possible reason is that the Pt/SSM CE possesses worse transmittance than Pt/PET CE, so the incident light via mesh pore of photoanode was weakened significantly after passing the mesh pore of Pt/SSM CE twice. Moreover, the incident light through photoanode is small part of total incident light [38]. Therefore, the improvement is not notable.

3.3. Counter electrodes

According to Table 3, the FDSSCs with Pt/SSM CE harvest higher conversion efficiency (2.84%) than that using Pt/PET CE (2.02%), which possibly results from higher conductivity, uniform distribution of Pt nanoparticles and higher catalytic ability.

Fig. 6(a) demonstrates the cyclic voltammetry (CV) curves of the Pt/SSM and Pt/PET CE at scan rate of 50 mV/s with an applied potential between -0.5 and 1.2 V in the acetonitrile solution composed of 9 mM LiI, 1 mM I_2 and 0.1 M $LiClO_4$. The Pt/SSM or Pt/PET, Pt mesh and Ag/Ag^+ electrode served as the working, counter, reference electrode respectively. From the CV curves it can observe two pairs of redox peaks. And peaks obtained at positive side are considered as anodic peak as well as peaks obtained at negative side are deemed as cathodic peak for Pt/SSM or Pt/PET. For the CV curve, cathodic peak refers to the reduction of tri-iodide and anodic peaks correspond to the oxidation of iodide and tri-iodide. The Pt/SSM showed both a larger oxidation and reduction current density than those of the Pt/PET electrode, suggesting a fast rate of tri-iodide reduction [39].

The EIS and corresponding parameters (insert image of Fig. 6(b)) of different CEs was exhibited in Fig. 6(b). In terms of EIS, Pt/SSM CE (8.71Ω) shows lower R_1 (transfer resistance at the CE/electrolyte interface) than that of Pt/PET CE (11.31Ω), which confirms Pt/SSM CE has stronger capability for electrocatalytic reduction of I_3^- to I^- ions in electrolyte as compared to Pt/PET CE [40].

Tafel polarization measurement is used to reconfirm the catalytic activity of Pt/SSM and Pt/PET CE. Fig. 6(c) shows the Tafel curves for symmetrical cells based on two electrodes (Pt/SSM and Pt/PET CE). The electrolyte in FDSSCs is employed to fabricate symmetrical cells. In the Tafel polarization curve, the exchange current density (J_0) is a direct measure of the electron transfer kinetics at the CE/electrolyte interface under equilibrium conditions, which can be obtained from the intercept of the extrapolated linear region of anodic or cathodic branch when the over potential is zero [41]. The higher J_0 value indicates a better catalytic activity. It can be observed that Pt/SSM CE has large value than Pt/PET CE, which means that Pt/SSM CE has better catalytic activity. The higher J_0 may result from the uniform distribution of Pt.

Fig. 7 demonstrates the tendency of the conversion efficiency generated from the FDSSCs which employed a Pt/SSM or Pt/PET CE and a TiO_2/ZnO NRs/SSM photoanode. After bend of 800 times with 90° bending angle, the Pt/SSM based device kept 70.1% of original conversion efficiency, and the Pt/PET based device maintained 58.4% of initial conversion efficiency. Therefore, it can be conformed that the Pt/SSM CE has better flexibility and stability than the Pt/PET CE.

Table 3
Photovoltaic characteristics of the DSSCs using different CE before and after attaching a reflecting film on the back of CE. Photoanodes: the TiO_2/ZnO NRs/SSM ($(NH_4)_2TiF_6$ treatment of 6 min).

Type	V_{oc} (V)	J_{sc} (mA. cm^{-2})	FF	Efficiency (%)
Pt/SSM	0.611	7.22	0.64	2.84
Pt/SSM@rf	0.616	7.98	0.63	3.12
Pt/PET	0.571	6.43	0.55	2.02
Pt/PET@rf	0.587	8.1	0.54	2.43

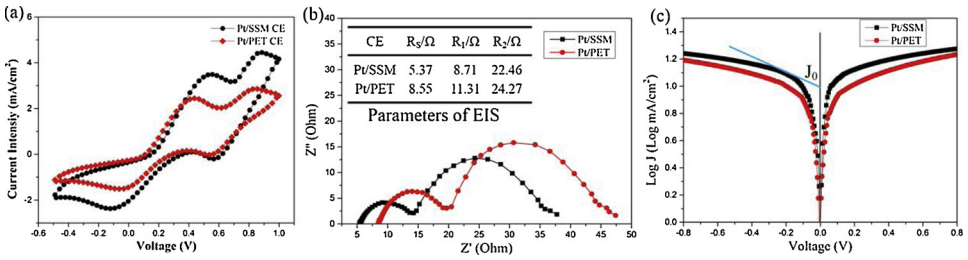

Fig. 6. (a) Cyclic voltammetry curves of Pt/SSM and Pt/PET CE at scan rate of 50 $mV.s^{-1}$ from -0.5 to 1.2 V in acetonitrile solution contained 9 mM LiI, 1 mM I_2 and 100 mM $LiClO_4$. Reference electrode: Ag/Ag^+. Counter electrode: Pt mesh. (b) EIS spectrum and corresponding parameters (insert image) of similar devices with different CEs. (c) Tafel polarization curves of Pt/SSM and Pt/PET CE obtained by the symmetrical cells and electrolytes were the same as used in DSSCs.

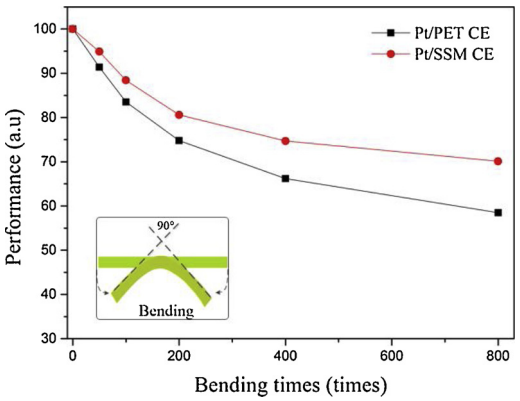

Fig. 7. The tendency of conversion efficiency generated from the FDSSCs with Pt/SSM or Pt/PET CE after various bending times at bending angle of 90°.

4. Conclusion

A full-SSM FDSSCs with a ZnO NRs/SSM photoanode and a Pt/SSM CE was fabricated by a simple process. But it failed to exhibit satisfying conversion efficiency. Subsequently, a TiO_2 buffer layer was introduced in situ on the surface of ZnO NRs via $(NH_4)_2TiF_6$ treatment. Thus, the recombination reaction was weakened and the photoexcited electron injection was improved significantly. The J_{sc}, V_{oc}, FF of device increased from 4.61 mA/cm^2, 0.49 V, 0.43 to 7.22 mA/cm^2, 0.61 V, 0.64 respectively. This research confirmed the TiO_2 buffer layer formed by $(NH_4)_2TiF_6$ treatment is feasible to reduce aggregation of dye molecule and improve conversion efficiency of ZnO FDSSCs when the ZnO photoanode is treated in a short time. The Pt/SSM also exhibited higher catalytic capability and longer stability under repeating bend. For a farther increase in conversion efficiency, a reflecting film also was introduced on the back of FDSSCs for improving light-utilizing ability. As a result, J_{sc} was increased to 7.94 mA/cm^2 from 7.22 mA/cm^2. Finally, a conversion efficiency of 3.12% was obtained. Although reflecting film accelerated the improvement in conversion efficiency, the effect of reflecting film was not notable to a full-SSM FDSSCs.

Acknowledgements

This research was supported by the National Natural Science Foundation of China (61674113, 51622507, and 61471255), Natural Science Foundation of Shanxi Province, China (2016011040), and Scientific and Technological Innovation Programs of Higher Education Institutions in Shanxi Province, China (2016138).

References

[1] B. O'Regan, M. Grätzel, A low-cost, high-efficiency solar cell based on dye-sensitized colloidal TiO_2 films, Nat. Mater. 353 (1991) 737–740.
[2] S. Ito, N.L.C. Ha, G. Rothenberger, P. Liska, P. Comte, S.M. Zakeeruddin, P. Péchy, M.K. Nazeeruddina, M. Grätzel, High-efficiency (7.2%) flexible dye-sensitized solar cells with Ti-metal substrate for nanocrystalline-TiO_2 photoanode, Chem. Commun. 38 (2006) 4004–4006.
[3] U.V. Desai, C. Xu, J. Wu, D. Gao, Hybrid TiO2–SnO2 nanotube arrays for dye-sensitized solar cells, J. Phys. Chem. C 117 (2013) 3232–3239.
[4] Z. Xue, L. Wang, B. Liu, Facile fabrication of co-sensitized plastic dye-sensitized solar cells using multiple electrophoretic deposition, Nanoscale 5 (2013) 2269–2273.
[5] X. Wang, Q. Tang, B. He, R. Li, L. Yu, 7.35% efficiency rear-irradiated flexible dye-sensitized solar cells by sealing liquid electrolyte in a groove, Chem. Commun. (Camb.) 51 (2015) 491–494.
[6] W. Maiaugree, P. Pimparue, W. Jarernboon, S. Pimanpang, V. Amornkitbamrung, E. Swatsitang, NiS(NPs)-PEDOT-PSS composite counter electrode for a high

efficiency dye sensitized solar cell, Mater. Sci. Eng. B 220 (2017) 66–72.
[7] F. Bella, D. Pugliese, L. Zolin, C. Gerbaldi, Paper-based quasi-solid dye-sensitized solar cells, Electrochim. Acta 237 (2017) 87–93.
[8] Y.Y. Bu, Novel ZnO decorated SnO_2 nanosheet for dye sensitized solar cell applications, Optik 157 (2018) 406–409.
[9] C. Gao, Q. Han, M. Wu, Review on transition metal compounds based counter electrode for dye-sensitized solar cells, J. Energy Chem. 27 (2018) 703–712.
[10] A.A. Kumar, J. Singh, D.S. Rajput, A. Placke, A. Kumar, J. Kumar, Facile wet chemical synthesis of Er^{3+} /Yb^{3+} co-doped $BaSnO_3$ nano-crystallites for dye-sensitized solar cell application, Mater. Sci. Semicond. Process. 83 (2018) 83–88.
[11] Z. Xu, T. Li, Q. Liu, F. Zhang, X. Hong, S. Xie, C. Lin, X. Liu, W. Guo, Controllable and large-scale fabrication of rectangular CuS network films for indium tin oxide-and Pt-free flexible dye-sensitized solar cells, Sol. Energy Mater. Sol. Cells 179 (2018) 297–304.
[12] M. Zalas, A. Cynarzewska, Application of paper industry waste materials containing TiO_2 for dye-sensitized solar cells fabrication, Optik 158 (2018) 469–476.
[13] M.S. Ahmad, A.K. Pandey, N. Abd Rahima, Advancements in the development of TiO_2 photoanodes and its fabrication methods for dye sensitized solar cell (DSSC) applications. A review, Renew. Sustain. Energy Rev 77 (2017) 89–108.
[14] W. Liu, H. Zhang, H. Wang, M. Zhang, M. Guo, Titanium mesh supported TiO_2 nanowire arrays/upconversion luminescence Er^{3+}-Yb^{3+} codoped TiO_2 nanoparticles novel composites for flexible dye-sensitized solar cells, Appl. Surf. Sci. 422 (2017) 304–315.
[15] M. Marandi, Z. Goudarzi, L. Moradi, Synthesis of randomly directed inclined TiO_2 nanorods on the nanocrystalline TiO_2 layers and their optimized application in dye sensitized solar cells, J. Alloys. Compd. 711 (2017) 603–610.
[16] N. Nyein, W.K. Tan, G. Kawamura, A. Matsuda, Z. Lockman, TiO_2 nanotube arrays formation in fluoride/ethylene glycol electrolyte containing LiOH or KOH as photoanode for dye-sensitized solar cell, J. Photochem. Photobiol. A: Chem. 343 (2017) 33–39.
[17] S.M.H. Al-Jawad, O.N. Salman, N.A. Yousif, Influence of titanium tetrachloride concentration and multiple growth cycles of TiO_2 nanorod on photoanode performance in dye sensitized solar cell, Photon. Nanostruct. – Fundam. Appl. 31 (2018) 81–88.
[18] Y. Xiao, J. Wu, C. Cheng, Y. Chen, G. Yue, J. Lin, M. Huang, L. Fan, Z. Lan, Low temperature fabrication of high performance and transparent Pt counter electrodes for use in flexible dye-sensitized solar cells, Chinese Sci. Bull. 57 (2012) 2329–2334.
[19] K.M. Lee, L.C. Lin, C.Y. Chen, V. Suryanarayanan, C.G. Wu, Preparation of high transmittance platinum counter electrode at an ambient temperature for flexible dye-sensitized solar cells, Electrochim. Acta 135 (2014) 578–584.
[20] Y.H. Wei, C.S. Chen, C.C.M. Ma, C.H. Tsai, C.K. Hsieh, Electrochemical pulsed deposition of platinum nanoparticles on indium tin oxide/polyethylene terephthalate as a flexible counter electrode for dye-sensitized solar cells, Thin Solid Films 570 (2014) 277–281.
[21] R. Vittal, K.C. Ho, Zinc oxide based dye-sensitized solar cells: a review, Renew. Sustain. Energy Rev. 70 (2017) 920–935.
[22] X. Wang, H. Lu, W. Liu, M. Guo, M. Zhang, Electrodeposition of flexible stainless steel mesh supported ZnO nanorod arrays with enhanced photocatalytic performance, Ceram. Int. 43 (2017) 6460–6466.
[23] A. Khan, Y.T. Huang, T. Miyasaka, M. Ikegami, S.P. Feng, W.D. Li, Solution-processed transparent nickel-mesh counter electrode with in-situ electrodeposited platinum nanoparticles for full-plastic bifacial dye-sensitized solar cells, ACS Appl. Mater. Interfaces 9 (2017) 8083–8091.
[24] H. Lu, X. Zhai, W. Liu, M. Zhang, M. Guo, Electrodeposition of hierarchical ZnO nanorod arrays on flexible stainless steel mesh for dye-sensitized solar cell, Thin Solid Films 586 (2015) 46–53.
[25] H. Dai, Y. Zhou, Q. Liu, Z. Li, C. Bao, T. Yu, Z. Zhou, Controllable growth of dendritic ZnO nanowire arrays on a stainless steel mesh towards the fabrication of large area, flexible dye-sensitized solar cells, Nanoscale 4 (2012) 5454–5460.
[26] K. Keis, J. Lindgren, S.E. Lindquist, A. Hagfeldt, Studies of the adsorption process of Ru complexes in nanoporous ZnO electrodes, Langmuir ACS J. Surf. Colloids 16 (2000) 4688–4694.
[27] H. Horiuchi, R. Katoh, K. Hara, M. Yanagida, S. Murata, H. Arakawa, M. Tachiya, Electron injection efficiency from excited N3 into nanocrystalline ZnO films: effect of (N3-Zn^{2+}) aggregate formation, J. Phys. Chem. B 107 (2003) 2570–2574.
[28] H. Dai, Y. Zhou, L. Chen, B. Guo, A. Li, J. Liu, T. Yu, Z. Zou, Porous ZnO nanosheet arrays constructed on weaved metal wire for flexible dye-sensitized solar cells, Nanoscale 5 (2013) 5102–5108.
[29] T.T. Vu, L. del Río, T. Valdés-Solís, G. Marbán, Fabrication of wire mesh-supported ZnO photocatalysts protected against photocorrosion, Appl. Catal. B: Environ. 140–141 (2013) 189–198.
[30] J. Cai, Z. Chen, S. Li, S. Dong, C. Wei, F. Li, Y. Peng, X. Jia, W. Zhang, A novel hierarchical ZnO-nanosheet-nanorod-structured film for quantum-dot-sensitized solar cells, Electrochim. Acta 274 (2018) 326–333.
[31] P.H. Joshi, D.P. Korfiatis, S.F. Potamianou, K.A.T. Thoma, Oxide thickness and roughness factor as parameters for TiO2-Dye sensitized solar cells performance, Russ. J. Electrochem. 47 (2011) 517–521.
[32] H.J. Kim, D.E. Kim, Effect of surface roughness of top cover layer on the efficiency of dye-sensitized solar cell, Sol. Energy 86 (2012) 2049–2055.
[33] S. Hernandez, V. Cauda, A. Chiodoni, S. Dallorto, A. Sacco, D. Hidalgo, E. Celasco, C.F. Pirri, Optimization of 1D ZnO@TiO2 core-shell nanostructures for enhanced photoelectrochemical water splitting under solar light illumination, ACS Appl. Mater. Interfaces 6 (2014) 12153–12167.
[34] D. Sengupta, P. Das, B. Mondal, K. Mukherjee, Effects of doping, morphology and film-thickness of photo-anode materials for dye sensitized solar cell application – a review, Renew. Sustain. Energy Rev. 60 (2016) 356–376.
[35] S. Illa, P. Basak, Polymer electrolyte integrated dye sensitized solar cells endow enhanced stability: photoanode thickness and light intensity on cell performance, Sol. Energy 169 (2018) 159–166.
[36] C. Vittoni, V. Sacchetto, D. Costenaro, S. Mastroianni, A. Hinsch, L. Marchese, C. Bisio, Gelation of solvent-free electrolyte using siliceous materials with different size and porosity for applications in dye sensitized solar cells, Sol. Energy 124 (2016) 101–113.
[37] R. Katoh, A. Furube, Electron injection efficiency in dye-sensitized solar cells, J. Photochem. Photobiol. C 20 (2014) 1–16.
[38] K. Sim, S.J. Sung, D.H. Kim, Light harvest properties of dye-sensitized solar cells with different spatial configurations of reflecting layer, J. Nanosci. Nanotechnol. 13 (2013) 7123–7126.
[39] R. Kumar, P. Bhargava, Synthesis and characterization of carbon based counter electrode for dye sensitized solar cells (DSSCs) using organic precursor 2-2′Bipyridine (Bpy) as a carbon material, J. Alloys. Compd. 748 (2018) 905–910.
[40] A. Sacco, Electrochemical impedance spectroscopy: fundamentals and application in dye-sensitized solar cells, Renew. Sustain. Energy Rev. 79 (2017) 814–829.
[41] F. Gong, H. Wang, X. Xu, G. Zhou, Z.S. Wang, In situ growth of Co0.85Se and Ni0.85Se on conductive substrates as high-performance counter electrodes for dye-sensitized solar cells, J. Am. Chem. Soc. 134 (2012) 10953–10958.